Hydrogen Autoignition at Pressures above the Second Explosion Limit (0.6–4.0 MPa)

DAEYUP LEE, SIMONE HOCHGREB

Department of Mechanical Engineering, Massachusetts Institute of Technology, Cambridge, Massachusetts 02139

Received 1 June 1997; accepted 7 October 1997

ABSTRACT: The investigation of high-pressure autoignition of combustible mixtures is of importance in providing both practical information in the design of combustion systems and fundamental measurements to verify and develop chemical kinetic models. The autoignition characteristics of hydrogen-oxygen mixtures at low pressures have been explored extensively, whereas few measurements have been made at high pressures. The present measurements extend the range of pressures up to 4 MPa, where few measurements have yet been reported.

Using a rapid compression machine equipped with a specially designed piston head, hydrogen autoignition pressure traces were measured at pressures above the second explosion limit (p = 0.6–4 MPa, T = 950–1050 K). The measured pressure records show a more gradual pressure increase during induction time in this regime than in the low-pressure regime, indicating that the energy release becomes significant at conditions over the second explosion limit.

By comparing the measurements and a thermodynamic model which incorporates the heat transfer and energy release, a modified reaction rate constant for $H_2O_2 + H = HO_2 + H_2$, one of the most important reactions for hydrogen oxidation at high pressure, and the reaction with the largest uncertainty, is suggested in this work as $k_{17} = 2.3 \cdot 10^{13} \exp(-4000/T)$ cm³/mol-s. The modeled pressure history with the modified reaction rate agrees well with the measured values during the induction period over the range of conditions tested. © 1998 John Wiley & Sons, Inc. Int J Chem Kinet 30: 385–406, 1998

INTRODUCTION

The study of high-pressure autoignition of combustible mixtures is of importance both as practical information in the design of combustion systems, as well as in providing fundamental measurements to verify and develop chemical kinetic models. The autoignition and explosion characteristics of hydrogen-oxygen mixtures at low pressures have been extensively in-

vestigated (Fig. 1). At low temperatures, an inverted "S" shaped curve divides the explosive and nonexplosive regions. The second explosion limit is defined by the competition of the branching and recombination pathways $H + O_2 \rightarrow OH + O$ (R1) and $H + O_2 + M \rightarrow H + O_2 + M$ (R9) as the total concentration [M] = 2 k_1/k_9. At higher pressures, secondary branching involving the formation and decomposition of H_2O_2 characterizes the third explosion limit. Within the explosive region, differences in the nature of the reaction have been experimentally observed in shock tubes as "weak" and "strong" ignition corresponding to a transition around the extended second limit [1–
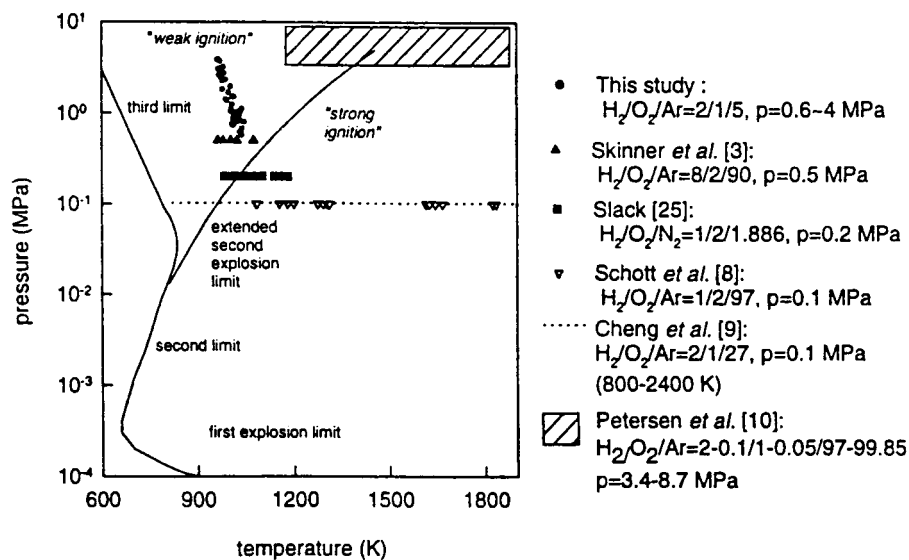
Figure 1 Present and previous range of measurements (all other measurements indicated are from shock tubes).

4]. Kordylewski and Scott [5] and Gray and Sherrington [6] suggested that the energy release during the induction time becomes significant at pressures above the second limit. Yetter et al. [7] reexamined the phenomena in the light of eigenvalue analysis to show that the transition from a weak to strong ignition corresponds to a change in the controlling reactions from reactions involving HO_2 to the usual high-temperature, low-pressure explosion mechanism involving the branching reaction $H + O_2 \rightarrow OH + O$ (R1).

Previous experimental studies using shock tubes determined autoignition times in the low-pressure, high-temperature, strong explosion region. Schott and Kinsey [8] investigated the range from 1080 to 1840 K at 0.1 MPa; Skinner and Ringrose [3] extended the range of temperatures to 964–1075 K at 0.5 MPa, determining a change in activation energy as the state of the mixture crosses the extended second limit, and Cheng and Oppenheim [9] obtained ignition delay times in the range of temperature from 800 to 2400 K and pressures from 0.1 to 0.3 MPa. More recently, Petersen et al. [10] investigated the ignition delay time of dilute H_2—O_2 in a shock tube at pressures up to 87 atm and temperatures between 1000–1800 K.

The present measurements reside in the weak ignition regime above the extended second explosion limit, at temperatures between 950 and 1050 K, and pressures up to 4 MPa, where no measurements had yet been made. Results of rapid compression machine measurements of autoignition of nondilute stoichiometric mixtures of H_2—O_2—Ar are described, along with a comprehensive analysis and comparison of model and experiments. The role of specific reactions, and that of early energy release are investigated. One of the key reactions (R17) is reevaluated, and a revised rate constant is suggested.

EXPERIMENTAL

The experiments were conducted in a rapid compression machine (RCM), whose detailed features are described elsewhere [11]. Briefly, the device allows a reactive mixture confined in a cylinder to be rapidly compressed (15–30 ms) by the motion of a piston, which is then locked into position. The ensuing pressure and temperature increase initiates the reaction, which proceeds in a constant volume chamber. The pressure in the chamber is measured throughout the process. The rapid compression minimizes the amount of reaction taking place prior to the peak pressure point, and the reaction can be effectively considered

Table I Experimental Parameters

Stroke L	7.47–9.98 cm
Clearance Height H	0.62 cm
Initial pressure p_0	0.015–0.12 MPa
Initial temperature T_0	297–299 K
Compression time t_c	20–30 ms
H_2/O_2/Ar	2/1/5[a]

[a] Purity levels: H_2-99.995%; O_2-99.6%; and Ar-99.998%.
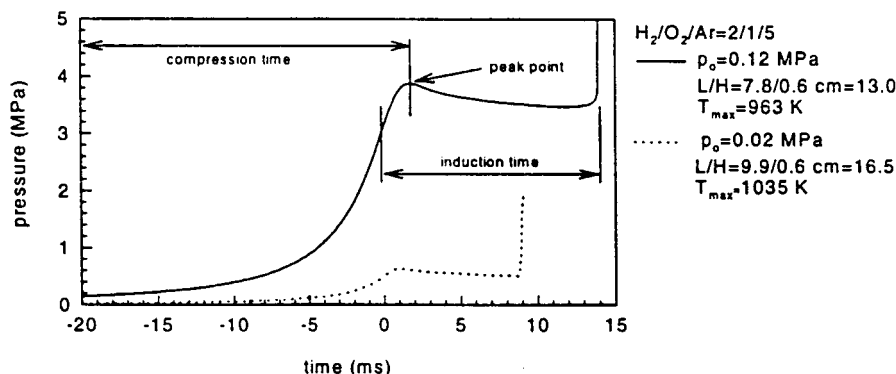
Figure 2 Typical measured pressure profiles for hydrogen-oxygen autoignition. Time zero is defined where the steepest pressure slope is obtained during compression process. The piston stops at the peak point (p_{max}, T_{max}).

to start at peak pressure and temperature conditions. Final pressures and temperatures can be controlled by varying the initial pressure, the compression ratio and the mixture composition.

One of the difficulties in interpreting RCM results has been the effect of disturbances to the reacting mixture by the rolling-up of a toroidal vortex containing the colder thermal boundary layer. A significant modification has been made to the original design by introducing a new piston geometry to minimize this disturbance. An extensive discussion of the new piston crevice design, as well as the heat transfer model during and after compression is presented in a separate article [12]. Comparison of model predictions and experiments suggests that the proposed crevice is effective in suppressing the corner vortex, allowing more accurate predictions of the reacting temperatures. A model incorporating the displacement history of the piston, the chamber geometry, and the thermodynamic and transport properties of the mixture is able to accurately predict the observed pressures from the initial conditions throughout the compression phase and the induction time.

Experiments were performed using $H_2/O_2/Ar$ mixtures at peak pressures between 0.6 to 4 MPa, and peak temperatures between 950 and 1050 K, with induction times of up to 45 ms. The experimental conditions are summarized in Table I. The initial pressure and stroke were varied, while other parameters such as the clearance height and gas mixture ratio were fixed. The single gas mixture was initially prepared as a ratio of $H_2/O_2/Ar = 2/1/5$ and loaded into the combustion chamber. Notice that this dilution ratio is much smaller than typically used in shock-tube measurements.

Pressures were measured with a Kistler piezoelectric transducer (Kistler 6123: range 200 bar, linearity

$\pm 0.2\%$) located on the bottom side of the combustion chamber. The voltage signal from a charge amplifier was stored in a PC through a data acquisition board (DT2821) and recorded digitally at a frequency of 100 kHz. The mixture was prepared by using a MKS 122A (range 0–1000 torr) diaphragm pressure gage with an accuracy of 0.1 torr.

EXPERIMENTAL RESULTS

Typical measured pressure histories within the experimental pressure and temperature range are shown in Figure 2. In both cases, the pressure rises through the compression period of the order of 20 ms. The peak pressure is determined by the initial pressure p_0 and temperature T_0, the compression ratio $r = L/H$ and the ratio of specific heats γ, via $p/p_0 \sim r^\gamma$, whereas the final temperature is controlled by $T/T_0 \sim r^{\gamma-1}$. There-
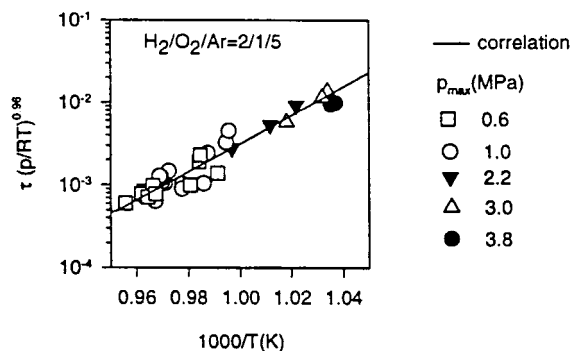
Figure 3 Measured induction times (symbols) and correlation (line) for peak. Temperature and pressure values (Units are in ms, MPa, and $\mathscr{R} = 8.314$ J/mol K) $\tau = (p/\mathscr{R}T)^{-0.96}$ 3.72×10^{-20} exp(39,000/T).

fore, pressure and temperature can be controlled independently by varying both the compression ratio and the initial pressure. The solid line shows a low-temperature, high-pressure case, with a longer ignition time than the dotted line, for the lower-pressure, higher-temperature case. Peak pressure and temperature are reached at the end of the piston travel. The pressure then drops as a result of heat transfer through the walls. Although not clearly visible in this picture, the higher-pressure, lower-temperature case shows a higher heat release prior to autoignition. Eventually, energy release due to reaction once again increases the pressure and temperature, leading to autoignition. Induction times used for comparison with model results are measured from the point of inflection in the compression trace to the inflection point during autoignition. The inflection point is used as the origin, since it is a better defined reference than the peak point (Fig. 2). Simulations performed using integration of chemical kinetics throughout compression to peak pressure showed no significant reaction prior to peak point. Therefore, comparison of calculated and measured induction times is made based on the comparison of experimental induction times from the steepest slope of compression with calculated times from peak pressure, with the addition of the interval (0.9 ± 0.3 ms) between steepest slope and peak.

The experimentally measured induction times are listed in Table A.I (see Appendix) and shown in Figure 3. Peak temperatures, T_{max}, were calculated by assuming that the core gases (i.e., the region away from the thermal boundary layer) are compressed adiabatically (The assumptions for the thermodynamic and reaction model are discussed in detail later).

$$\ell n\left(\frac{T}{T_0}\right) = \int_{p_0}^{p} \frac{\gamma(T) - 1}{\gamma(T)} \, d(\ell n \, p) \qquad (1)$$

Figure 3 shows the measured induction times (listed in Table A.I). All values can be correlated to concentration and temperature by $\tau = 3.72 \times 10^{-20}(p/\mathscr{R}T)^{-0.96} \exp(39,000/T)$ (units are ms, MPa, K, and $\mathscr{R} = 8.314$ J/mol K) with a correlation coefficient $r^2 = 0.92$. Uncertainties in the measurement of pressure ($\pm 0.2\%$) correspond to uncertainties of up to ± 1 K in peak temperatures. The repeatability of induction times for nominally identical conditions is ± 1 ms.

Ignition delay times, scaled to first-order with oxy-
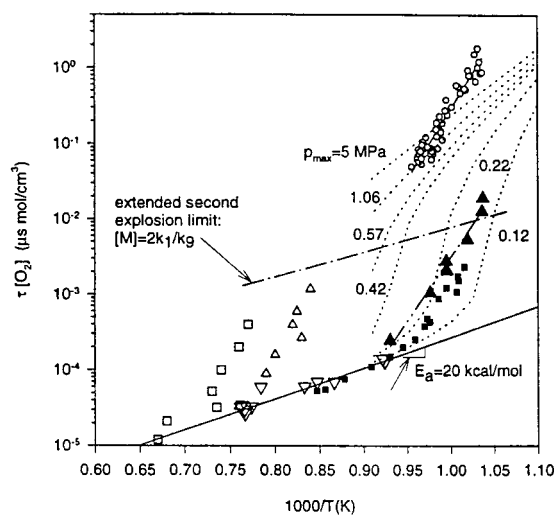
Figure 4   Measured induction times (scaled by O_2 concentrations for comparison with other measurements) as a function of reciprocal temperature.

○	This work:	$H_2/O_2/Ar = 2/1/5$,	$p = 0.6–4$ MPa
▲	Skinner et al. [3]:	$H_2/O_2/Ar = 8/2/90$,	$p = 0.5$ MPa
▽	Schott et al. [8]:	$H_2/O_2/Ar = 1/2/97$,	$p = 0.1$ MPa
■	Slack [25]:	$H_2/O_2/N_2 = 1/2/1.886$,	$p = 0.2$ MPa
—	Cheng et al. [9]:	$H_2/O_2/Ar = 2/1/27$,	$p = 0.2$ MPa
△	Petersen et al. [10]:	$H_2/O_2/Ar = 2–0.1/1–0.05/97–99.85$,	$p = 3.4$ MPa
□			$p = 6.5$ MPa
----	adiabatic calculation:	$H_2/O_2/Ar = 2/1/5$ (rate constants Table II)	

gen concentrations for comparison with previous experiments, are plotted as a function of reciprocal temperatures in Figure 4. Clearly, most of the measurements have been made below the second extended explosion limit represented by $[M] = 2k_1/k_9$. The experimental results show that at high temperatures and low pressures, the apparent activation energy is relatively low (20 kcal/mol). At low temperatures and high pressures, the measured apparent activation energy in the present experiments is of the order of 70 kcal/mol. Calculations performed using an adiabatic, constant volume chemical kinetic model provide guidance for the interpretation of the experimental results. Although not directly comparable to the experimental data because of heat losses, the model clearly shows two distinct limits at low and high concentrations, and a switch-over region with a high apparent activation energy. In the following discussion, it is shown that the behavior of a nondilute hydrogen-oxygen system within the explosive regime is very different at low pressures than at high pressures. As will be shown later, the heat release associated with exothermic reactions involving HO_2 is critical in determining the evolution of the reaction under nondilute high-pressure initial conditions.
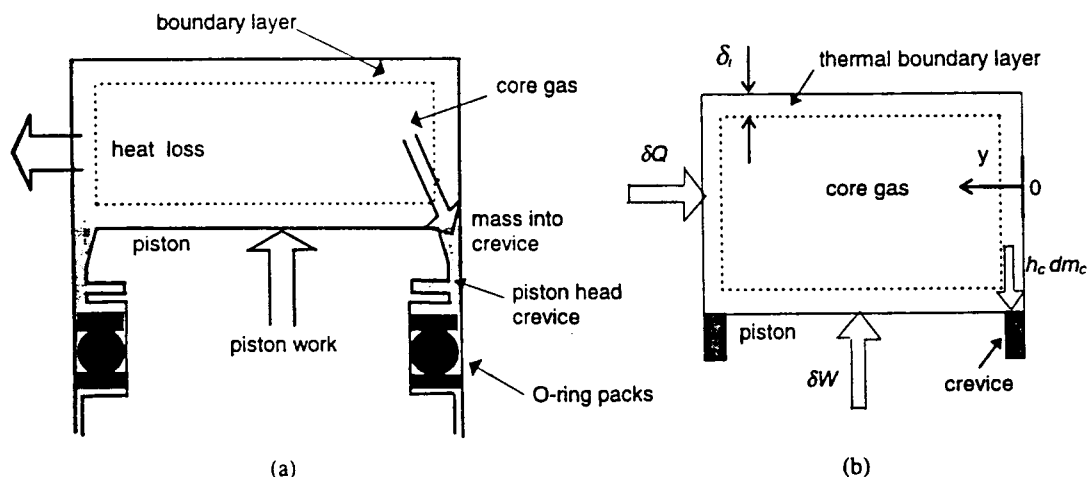
MODEL

In order to adequately model the detailed chemical kinetics of the reacting system for comparison with experimental measurements, the state of the reacting mixture must be accurately known. If induction times are relatively short, heat losses can be neglected, as some investigators have assumed. In this case, a constant volume reaction model is adequate, and a more complex chemical kinetic model can be used in simulations [13]. At the other extreme, the detailed fluid motion can be modeled using multidimensional computations coupled with a relatively simple chemical kinetic model [14–16]. In either case, the highly temperature sensitive nature of chemical kinetics requires precise understanding of the core gas behavior, since most of the reaction takes place there.

In RCMs with conventional crevice designs, the state of the core mixture and the heat transfer are affected by the motion of the rolled-up boundary layer as the piston travels. The present device avoids that effect, and, hence, creates well defined core gas conditions, by virtue of its piston head crevice design, which can contain the thermal boundary layer. The simplification of the fluid mechanics and heat transfer allows the use of detailed chemical kinetics for analysis at little computational expense. In what follows, a simple analytical model is described for determining the evolution of the thermodynamic state of the gas in the system throughout the compression and induction time, based solely on knowledge of the geometry of the chamber, the compression time, and gas properties. The model is combined with a chemical kinetic mechanism to simulate the effect of heat transfer on the core temperatures during autoignition. A discussion of the details involved, in the verification of the heat transfer model performance, is provided in Lee and Hochgreb [12].

The reacting mixture in a RCM is composed of a

Figure 5 Schematic of cylinder and piston head crevice. (a) Piston diagram (not to scale). (b) Schematic diagram of thermodynamic model. $\delta Q(<0)$ represents heat transfer through the wall. $\delta W(<0)$ denotes work done by the system. The mass dm_c represents transfer to crevice volume.

core gas region, defined as the central region of the gas, undisturbed by heat transfer to the walls, and the thermal boundary layer, which is the region near the walls where temperature gradients are large, and through which most of the heat transfer takes place (Fig. 5).

Model Assumptions

The assumptions used in the thermodynamic model of the RCM are as follows: (a) the system consists of three interacting regions: core, thermal boundary layer, and crevice. Energy transfers from the core are purely reversible transfers of work and mass with the piston and boundary layer. The crevice exchanges mass exclusively with the thermal boundary layer; (b) the thermal boundary layer thickness is small compared to the chamber dimensions, so that a one dimensional model can be employed (The calculated boundary layer thickness $\delta_{99\%}$ reaches a minimum of about 3% of the clearance height at maximum pressure, and a value of up to 15% of the clearance height prior to autoignition for the longest induction times.); (c) no chemical reaction takes place in the boundary layer. Because of the exponential nature of reaction rates, it can be shown that reaction rates within the boundary layer are much slower than in the core, except for a region within around 20% of the boundary layer thickness. It can also be shown that the calculated induction times are not particularly sensitive to this assumption; (d) heat transfer is controlled by heat conduction from the core gases to the wall. The flow velocity near the wall during compression process is low except near the crevice entrance, where convective heat transfer is assumed to be smaller than conduction. (The redesign of the crevice gap leads to excellent agreement of the calculated pressures with this assumption [12]); (e) the thermal boundary layer thickness is smaller than the entrance gap of a piston head crevice, and the length of a crevice is long enough to cool down the entering gas, so that the gas in the piston head crevice is nearly isothermal, at the same temperature as the walls. (The crevice gap width and profile was designed with these constraints in mind.); (f) surface reactions and thermal diffusion are negligible; (g) uniform pressure; (h) the gas is ideal: verified via the compressibility factor, even at the highest pressures; (i) the chamber walls remain at the initial temperature T_0. The approximation is valid for the metal surfaces surrounding the chamber; (j) the crevice gas is isothermal. The crevice is designed for quick cooling of the incoming boundary layer mass during compression; (k) the ratio of specific heats (γ) is a function

temperature only (ideal gas); (l) the gas constant R is uniform: $R_\infty = R_\delta = R_c = R$. This is valid up to the ignition point, since the composition hardly changes; and (m) the piston head crevice consists of the volume between the piston and the cylinder wall, above the O-ring packs which seal the combustion chamber.

The energy and mass balance equations are derived for each region (core, boundary layer, and crevice) and solved simultaneously to yield the pressure history in the chamber, and the evolution of the thermal boundary layer is calculated.

(i) System
Mass conservation (overall):

$$m = m_\infty + m_\delta + m_c \quad \text{or}$$
$$dm_\infty = -d(m_\delta + m_c) \quad (2)$$

Volume history ($V = V(t)$):

$$V = V_\infty + V_\delta \quad \text{or} \quad dV_\infty = dV - dV_\delta \quad (3)$$

(ii) Core volume
Energy conservation (reversible transfers):

$$dU_\infty = -p \, dV_\infty + h_\infty \, dm_\infty \quad (4)$$

where the internal energy for the core volume can be represented by:

$$dU_\infty = d(m_\infty u_\infty) \quad (5)$$

and the specific internal energy can be calculated from

$$u_\infty = \sum_{i=1}^{K} h_i Y_i - \frac{p}{\rho_\infty} \quad (6)$$

where the specific enthalpy is

$$h_i = h_{f,i}^{\ 0} + \int_{T_{\text{ref}}}^{T_\infty} c_{p,i} \, dT \quad (7)$$

Species conservation equation:

$$\frac{dY_i}{dt} = \frac{\dot{w}_i M_i}{\rho_\infty} \quad (8)$$

Core mass (state equation):

$$m_\infty = \rho_\infty V_\infty = \frac{p}{R_\infty T_\infty} V_\infty \quad (9)$$

(iii) Thermal boundary layer
The thermal boundary layer mass grows as $-dm_\infty$ is transferred from the core with enthalpy h_∞. Additional

mass is transferred to or from the isothermal crevice. Energy conservation:

$$dU_\delta = \delta Q - p \, dV_\delta - h_\infty \, dm_\infty - h_c \, dm_c \quad (10)$$

where conduction heat transfer through the cylinder wall is

$$\delta Q = -k_w A \left.\frac{dT}{dy}\right|_{y=0} dt \quad (11)$$

A is the area over which heat is being lost: the sum of piston, head, and side wall areas. The thermal conductivity k_w, is evaluated at the wall.
Boundary layer mass (for thin boundary layer):

$$m_\delta = \rho_\delta A \delta_t = A \int_0^{\delta_t} \frac{p}{RT} \, dy \quad (12)$$

Average boundary layer enthalpy:

$$h_\delta = \frac{A}{m_\delta} \int_0^{\delta_t} \rho c_p T \, dx = \frac{pA}{m_\delta} \int_0^{\delta_t} \frac{\gamma}{\gamma - 1} \, dy \quad (13)$$

(iii) Crevice
Mass leaves the isothermal crevice after peak pressure according to:

$$dm_c = d\left(\frac{V_c}{RT_c} p\right) \quad (14)$$

where V_c is a known function.*
Enthalpy of mass exchanged with crevice:

$$h_c \equiv \begin{cases} h_\delta & dm_c > 0 \\ h_o & dm_c < 0 \end{cases}' \quad (15)$$

From the given $V(t)$, the dependent variables p, T_∞, δ_t and Y_i can be calculated by solving the above equations simultaneously. Equations (1)–(15) were reduced to $(3 + K)$ equations to find $(3 + K)$ dependent variables. The resulting equations are summarized in Table A.II (see Appendix).

A final assumption must be made regarding the temperature profile within the boundary layer, so that its thickness, mass, and the average enthalpy can be calculated. The simple case of compression or expansion with an adiabatic core has been solved by Keck [33] yielding the following temperature profile:

---

* The crevice volume V_c increases slightly with time due to shift of O-ring packs, according to $V_c(t) = V_{co} + a(1 - \exp(-t^b/c))$, where $V_{co} = 1.32$ cm³, $a = 1.37$, $b = 0.6$, $c = 15.0$, and t(ms) is the time from peak pressure). Refer to ref. [12] for details.

$$\frac{T(\eta, t)}{T_\infty(t)} = 1$$
$$+ \int_0^t erfc\left(\frac{\eta}{2}\left(\alpha_w \int_{t'}^t \left(\frac{p''}{p_o}\right) dt''\right)^{-1/2}\right) \frac{d}{dt'}\left(\frac{T_0}{T_\infty}\right) dt' \quad (16)$$

where time zero is here the initial time before compression, and the scaled space coordinate is:

$$\eta(x, t) = \int_0^x \frac{\rho'}{\rho_o} \, dy' \quad (17)$$

It can be shown that the nondimensionalized temperature (Fig. 6) defined below is independent of time for a given gas mixture, so that it is only a function of the normalized distance y/δ_t

$$\theta(t) = \frac{T(\eta, t) - T_w}{T_\infty(t) - T_w} = f\left(\alpha_w, \frac{y}{\delta_t}\right) \quad (18)$$

Therefore, for the reacting case, it is reasonable to assume that the profile remains self-similar even though the core temperatures may rise as a result of chemical reaction thus, increasing the overall (nonnormalized) heat transfer.

Reaction Rate Mechanism

The chemical kinetic mechanism (10 species, 19 reactions) used in determining the evolution of the reaction and the reaction time was taken from Kim et al. [17], since that mechanism has been recently compared to high-pressure flow reactor data, at pressures
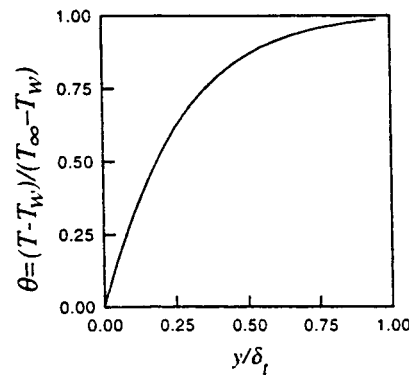
Figure 6 Nondimensionalized temperature profile within boundary layer for all times. δ_t denotes the thermal boundary layer thickness at the point where the temperature reaches 99% of the temperature difference with the wall. Note that the profile is time-independent. $H_2/O_2/Ar = 2/1/5$. α_w was calculated at $p_o = 0.067$ MPa and $T_o = 299$ K.

Table II   Reaction Rate Constants [17]

Reactions	A[a]	n	E_a	UF[b]	T[d]	$\Delta h_{(1000 \text{ K})}$
1. $H + O_2 = O + OH$	1.91E + 14	0.00	16.44	2	962–2,577	15.1
2. $O + H_2 = H + OH$	5.13E + 04	2.67	6.29	1.5	297–2,495	13.5
3. $OH + H_2 = H + H_2O$	2.14E + 08	1.51	3.43	1.5	250–2,581	−9.4
4. $O + H_2O = OH + OH$	2.95E + 06	2.02	13.4	2.5	250–2,000	2.9
5. $H_2 + M = H + H + M$[c]	4.57E + 19	−1.40	104.38	3	600–2,000	112.9
$H_2 + Ar = H + H + Ar$	5.89E + 18	−1.10	104.38			
6. $O + O + M = O_2 + M$	6.17E + 15	−0.50	0.00	1.3	2,000–10,000	−114.4
$O + O + Ar = O_2 + Ar$	1.91E + 13	0.00	−1.79			
7. $O + H + M = OH + M$	4.68E + 18	−1.00	0.00	10		− 99.3
8. $H + OH + M = H_2O + M$	2.24E + 22	−2.00	0.00	2	1,000–3,000	−122.3
$H + OH + Ar = H_2O + Ar$	8.32E + 21	−2.00	0.00			
9. $H + O_2 = HO_2$[g]	4.47E + 13	0.00	0.00			
$H + O_2 + M = HO_2 + M$	6.17E + 19	−1.42	0.00	3	200–2,000	46.9
$H + O_2 + Ar = HO_2 + Ar$	1.51E + 15	0.00	−1.00			
10. $HO_2 + H = H_2 + O_2$	6.61E + 13	0.00	2.13	2	298–773	−66.0
11. $HO_2 + H = OH + OH$	1.70E + 14	0.00	0.87	2	298–773	−37.4
12. $HO_2 + O = OH + O_2$	1.74E + 13	0.00	−0.40	1.2	200–400	−52.5
13. $HO_2 + OH = H_2O + O_2$	1.91E + 16	−1.00	0.00	2	254–1,050	−75.4
14. $HO_2 + HO_2 = H_2O_2 + O_2$[e]	4.17E + 14	0.00	11.98	3	650–850	−42.4
	1.29E + 11	0.00	−1.63			
15. $H_2O_2 = OH + OH$[g]	2.95E + 14	0.00	48.4			
$H_2O_2 + M = OH + OH + M$	1.20E + 17	0.00	45.5	2	700–1,500	51.9
$H_2O_2 + Ar = OH + OH + Ar$	1.91E + 16	0.00	43.0			
16. $H_2O_2 + H = H_2O + OH$	1.00E + 13	0.00	3.59	3	283–800	−70.4
17. $H_2O_2 + H = H_2 + HO_2$	4.79E + 13	0.00	7.95	5	283–800	−23.6
18. $H_2O_2 + O = OH + HO_2$	9.55E + 06	2.00	3.97	3	250–800	−10.1
19. $H_2O_2 + OH = H_2O + HO_2$[e]	1.00E + 12	0.00	0.00	2	250–1,250	−33.1
	5.80E + 14	0.00	9.56			

[a] Units are cm³, mol, s kcal, and K; $k = AT^n \exp(-E_a/RT)$.

[b] UF is an estimated uncertainty factor for the specified T range: $+\Delta k/k$ = UF-1 and $-\Delta k/k$ = 1/UF-1.

[c] Collision efficiencies: ϵ_{H2O} = 12; ϵ_{H2} = 2.5; and ϵ_{Ar} = 0.75. All other species have efficiency equal to unity.

[d] Temperature range over which the rate constant parameters are evaluated.

[e] Reaction rate constants for reactions 14 and 19 are the sums of the two rate constants.

[f] Refernces—reaction 1: Pirraglia et al. [20]; 2: Sutherland et al. [21]; 3: Michael et al. [22]; 4: Sutherland et al. [23]; 5, 6, 7, 8, 10, 11, 18, and 19: Tsang et al. [24]; 9: Slack [25], Baulch et al. [26], and Cobos et al. [27]; 14: Hippler et al. [28]; 15: Warnatz et al. [29] and Brouwer et al. [30]; 16: Warnatz et al. [29]; and 19: Hippler et al. [31].

[g] Pressure-dependent fall-off expressions are given as a Lindemann fit [38].

up to 1 MPa. The reaction rate constants are listed in Table II.

The standard thermodynamic properties used are listed in Table III. All values are taken from Kee et al. [18], with the exception of the heat of formation of HO_2 ($\Delta h_{f,298.15 \text{ K}}^0$ = 3.5 ± 0.5 kcal/mol by Shum and Benson [19], instead of $\Delta h_{f,298.15 \text{ K}}^0$ = 2.5 kcal/mol [18]). Note that Kim et al. used 3.0 kcal/mol [17].

The resultant pressure history was calculated using a modified Chemkin driver [18] combined with the thermodynamic model described in the previous section.

**Table III**   Thermodynamic constants at 298.15 K (Δh_f^0 in kcal/mol; Δs_f, c_p in cal/mol)

| Species	Δh_f^0	Δs_f^0	c_p
H	52.07	27.37	4.97
O	59.52	38.66	5.23
OH	9.31	43.71	9.85
H_2	0	31.12	6.90
O_2	0	48.93	7.01
H_2O	−57.77	44.52	7.99
HO_2	3.50	54.59	8.37
H_2O_2	−32.51	55.61	10.41
Ar	0	36.96	4.97

MODEL RESULTS

Before discussing model results, it is useful to review the mechanism of hydrogen ignition at low pressures (below the extended second limit) and high pressures (above the second limit). It can be shown that along

that transition the mechanism changes from a fully branched mechanism [7] (strong ignition below the pressures corresponding to the second limit) to a straight-chain mechanism with rare branching, where chemical energy release plays an important role (weak ignition).

(a) p=0.1 MPa

(b) p=0.3 MPa

(c) p=1.0 MPa
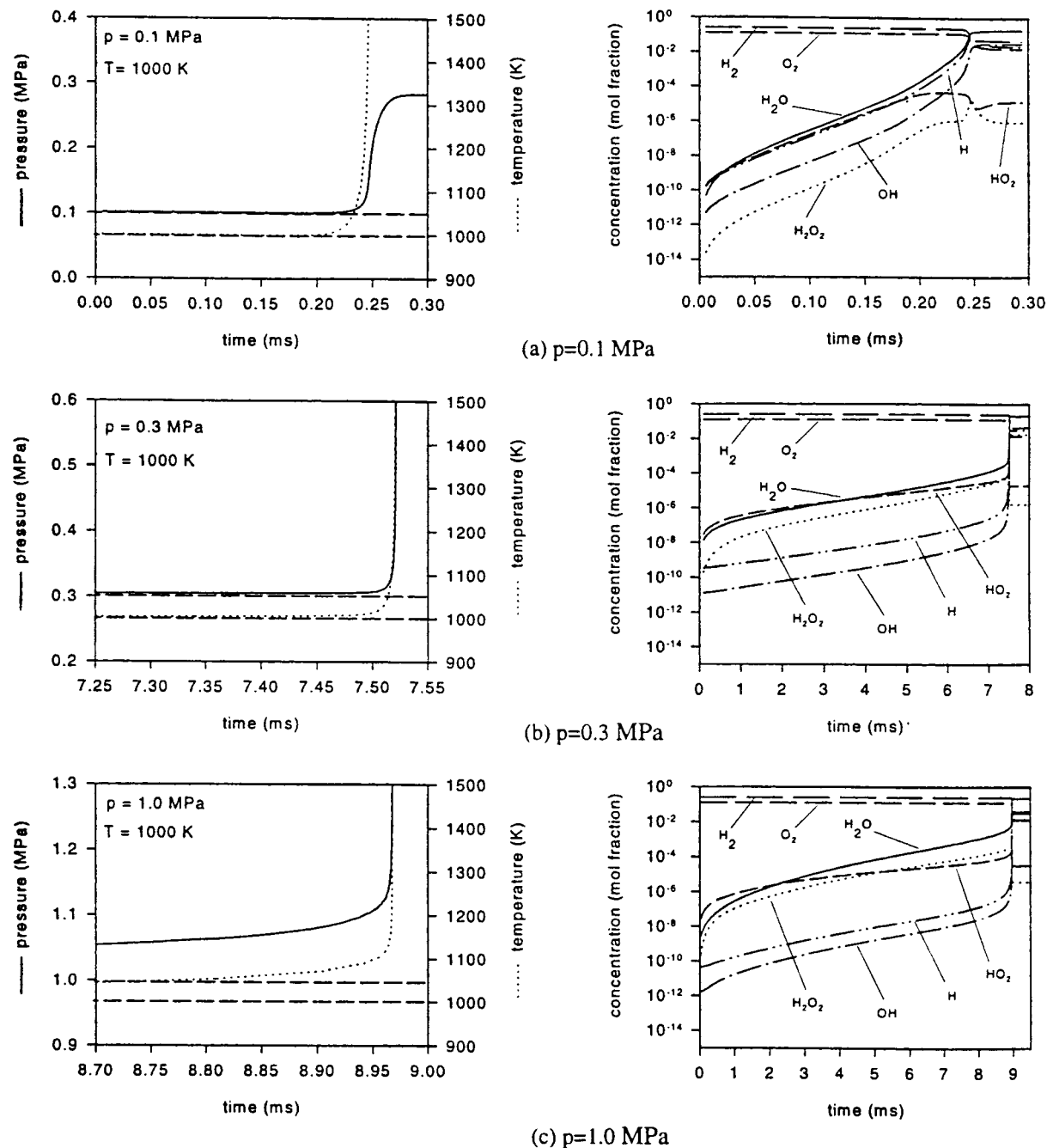
Figure 7 Pressure, temperature, and species concentration as a function of initial pressure for adiabatic, constant volume calculation at initial temperature $T = 1000$ K. Base reaction set from Table II. Initial pressures: (a) $p = 0.1$ MPa, (b) $p = 0.3$ MPa; and (c) $p = 1.0$ MPa. Note that pressure, temperature, and time spans are the same for all pressure profiles for comparison of energy release before autoignition.
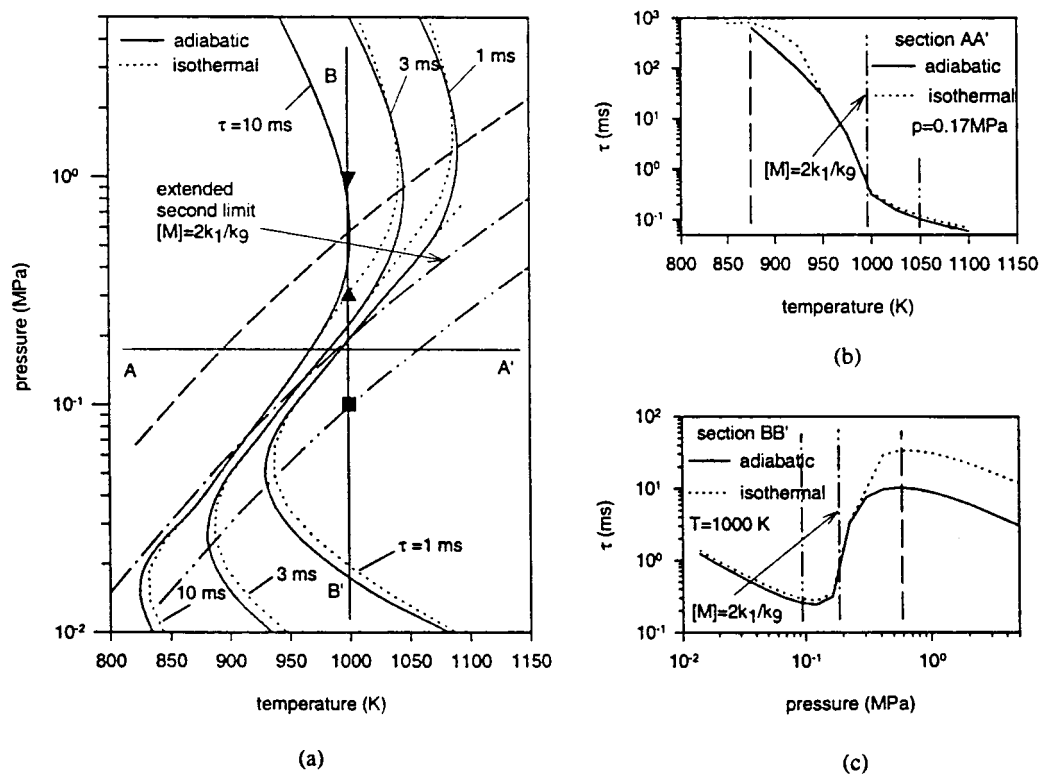
Figure 8 Induction time contour plots for hydrogen oxidation as a function of pressure and temperature. Symbols ■, ▲, and ▼ represent pressure and temperature conditions where calculations in Figure 7 were made (respectively, (a), (b), and (c)).
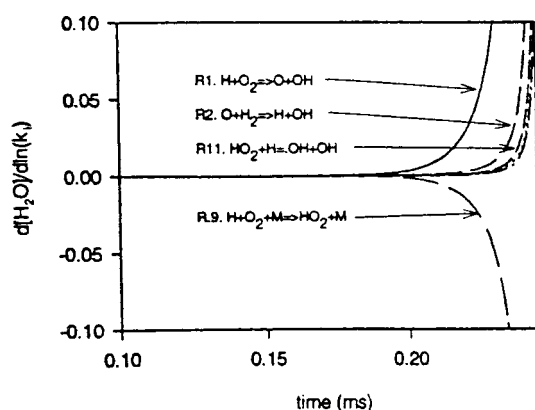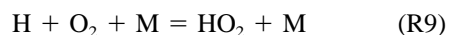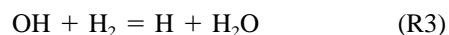
The characteristics of thermal explosion below and above the extended second explosion limit can be discussed in the context of the behavior an adiabatic, constant volume system starting at a temperature of 1000 K, but different initial pressures (Fig. 7). Below the extended second limit (Fig. 7(a)), temperature and pressure remain essentially constant throughout the induction period, indicating that energy release is not significant. At the other extreme above the second limit (Fig. 7(c)), both pressure and temperature rise due to early energy release. The concentration profiles reflect the corresponding characteristics depending on the initial pressure. Note that the increase in the concentrations of HO_2 and H_2O_2 radicals is more pronounced at high pressure (c) than at low pressure (a).

In order to understand the origin of these different characteristics, the comparison can be made between an isothermal and an adiabatic calculation in pressure and temperature space: In the isothermal case (dotted line in Fig. 8) both pressure and temperature are kept constant. The induction time is here defined at the point where the H_2O concentration peaks. In the adiabatic case, the reaction evolves from the initial temperature and pressure without heat loss at constant vol-

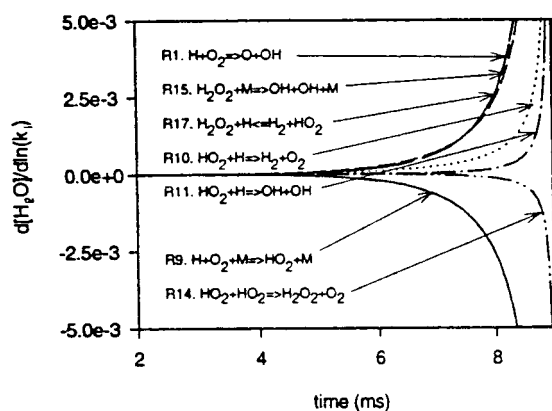ume (solid line in Fig. 8), and the induction time is calculated at the point where the rapid pressure rise occurs (it is also where the H_2O concentration peaks). Clearly, at pressures up to the extended second explosion limit, both isothermal and adiabatic calculations yield similar induction times. However, at high pressures, the induction time in the isothermal calculation is significantly longer than that in the adiabatic case (Fig. 8(c)), showing that the early energy release due to reaction plays a much more important role. This comparison between isothermal and adiabatic calculations shows that as pressure increases and temperature decreases across the extended second limit, energy release becomes significant during the induction time. Kordylewski et al. [5] investigated the influence of self-heating in the second and third explosion limits in the hydrogen oxidation system. They proposed that as the reactant pressure is increased toward the third limit, self-heating becomes important and influences the reaction rate mainly via the kinetics of hydrogen peroxide decomposition. The following analysis elucidates the pathways through which energy is released, as well as the reactions to which the induction time is most sensitive.
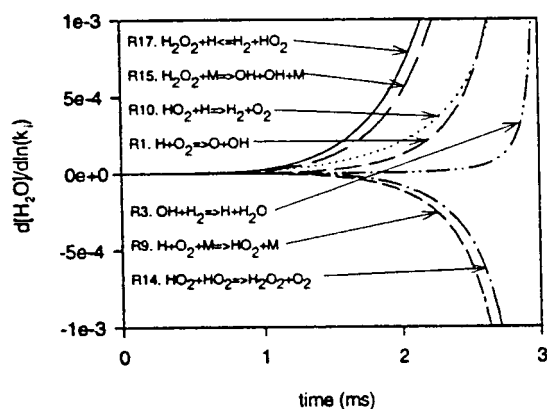
Reaction Pathways

The pathways of hydrogen oxidation at low pressures have been extensively investigated: at very low pressures, the overall reaction is dominated by reactions R1, R2, and R3 [32,34] (Refer to Table II for reaction numbers).

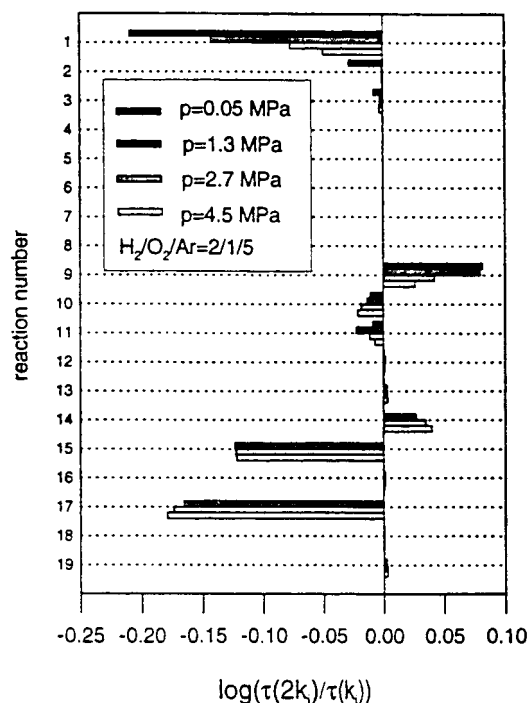$$H + O_2 = O + OH \qquad (R1)$$

$$O + H_2 = H + OH \qquad (R2)$$

$$OH + H_2 = H + H_2O \qquad (R3)$$

$$H + O_2 + M = HO_2 + M \qquad (R9)$$


Figure 9 Sensitivity analysis for H_2O as (a) $p = 0.1$ MPa, (b) 1.0 MPa, and (c) 5 MPa. $T_0 = 1000$ K for all cases. Sensitivity gradient is defined as $S_{ij} = k_j[\partial C_i/\partial k_j] = \partial C_i/\partial[\ln k_j]$, where C_i is the molar concentration for species i, and k_j is the preexponential factor for jth reaction.

Figure 10 Sensitivity of τ to different reaction rate constants. $\tau(2\,k_i)$ refers to induction time after an increase in the rate coefficient of the reaction and its reverse by a factor of two. Initial temperature in calculation $T = 1000$ K.

Below the extended second limit, the ratio of R1 to R9 controls the overall reaction rate, with R1 as the branching step and R9 the terminating step. As the pressure is increased, R9 becomes part of a chain propagating path (involving HO_2, H_2O_2) consisting essentially of reaction R9, R14, and R15 or reaction R9, R17b,* and R15.

$$HO_2 + HO_2 = H_2O_2 + O_2 \qquad (R14)$$

$$H_2O_2 + M = OH + OH + M \qquad (R15)$$

$$HO_2 + H_2 = H_2O_2 + H \qquad (R17b)$$
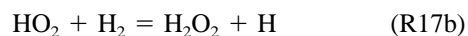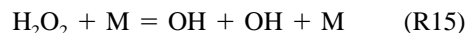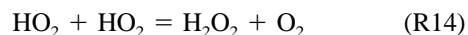
Sensitivity analysis of the overall reaction, as indicated by the sensitivity of water concentration (Fig. 9), and the sensitivity of the calculated induction time to the various reaction rate constants (Fig. 10) show that at high pressures, reactions R1–R3 are much less important than the reactions involving HO_2. These seven reactions can be grouped as the most important reactions over the whole pressure range.

---

* b denotes backward direction from stated in Table II.

Flux analyses of the origin and fate of HO_2 and H_2O_2 at various pressures (Fig. 11) show that as the pressure increases, HO_2 recombines into H_2O_2, followed by thermal decomposition of H_2O_2 into OH. Although both reactions R14 and R17b contribute to produce the H_2O_2, an increase in reaction rate constant for R17b accelerates the overall reaction, whereas an increase in R14 retards the overall reaction. This can be understood by considering the pathways leading to produce the OH radical at high pressure: The main branching pathway for production of OH radicals is the decomposition of H_2O_2. The latter is produced by the recombination of HO_2 molecules (R14) or abstraction of H from H_2 by HO_2 (R17b). These two paths are competing for HO_2. When R14 is increased, the overall rate of production of H_2O_2 is decreased (since it is in parallel with R17b, and consumed two HO_2) and this slows down the overall reaction.
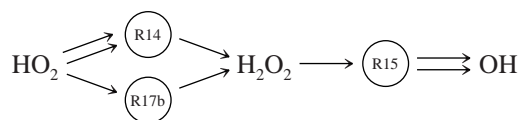

Figure 12 summarizes the low- and high-pressure pathways for the autoignition of hydrogen, which is composed of 9 main reactions, including the ones listed above, with the addition of R10 and R11. Ignition pressure and temperature histories calculated using the 9-reaction set are identical to those using the full set for pressures from 0.05 to 6 MPa. One last consideration must be made, however, regarding the role of early energy release during the induction time.

THERMAL ENERGY RELEASE

Slow competing reactions can become important if they are very exothermic, by significantly increasing the temperature of an (adiabatic) system and moving the system into an explosive regime. The largest contributions to the heat release (expressed as $\dot{w}_j \Delta h_j + r$ for each reaction j) are shown in Figure 13 for increasing pressures. At low pressures (below the extended explosion limit), heat release takes place only very late in the reaction, with the main exothermic reaction being R3, the reaction of OH with H_2. As the pressure increases, the contribution of the exothermic self-reaction of HO_2 contributes a significant fraction of the energy release, moderated by the highly endothermic decomposition of H_2O_2. The relevant exothermic reaction paths are:
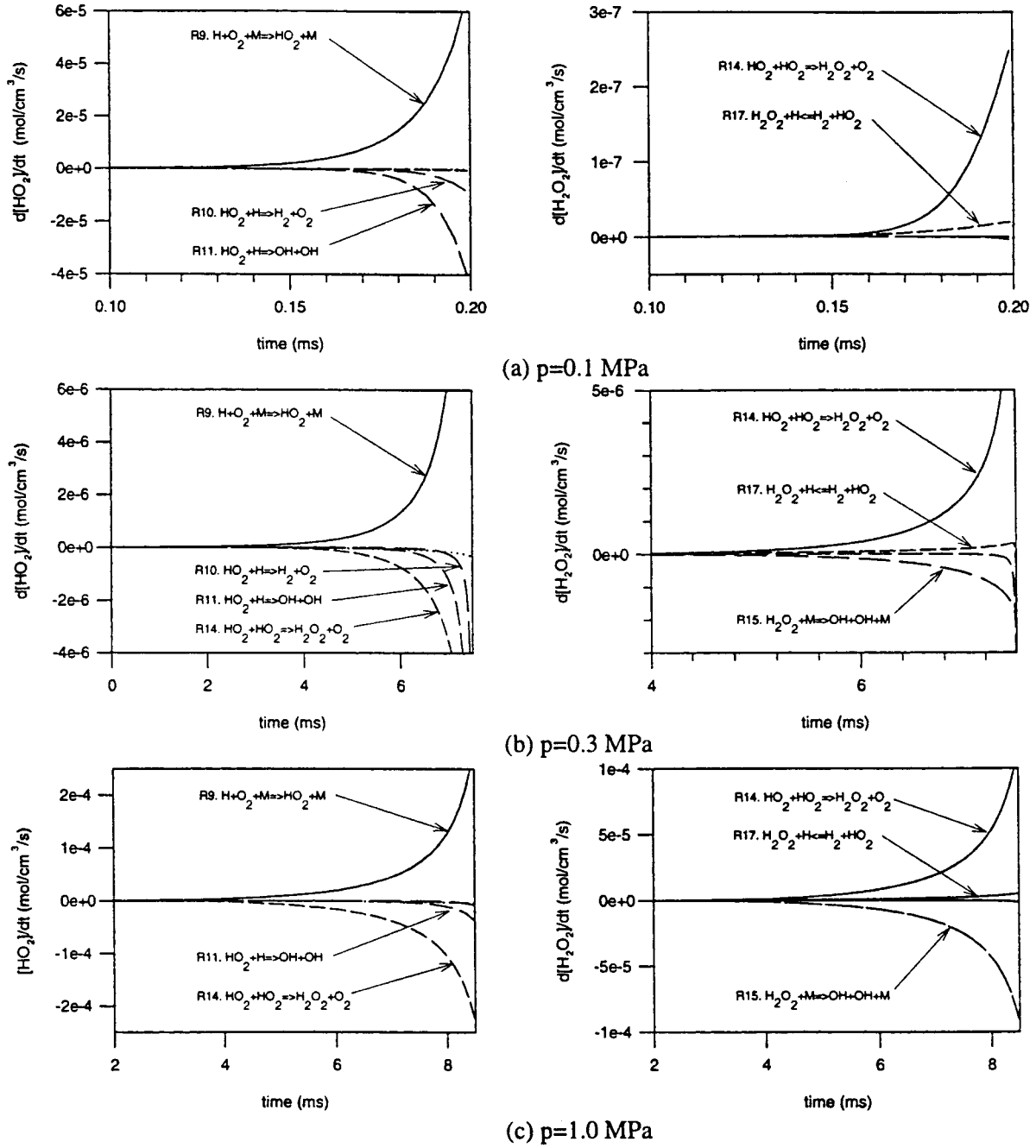
Figure 11   Flux analysis for HO_2 and H_2O_2 as for different initial pressures: (a) 0.1 MPa, (b) 0.3 MPa, and (c) 1.0 MPa. Initial temperature $T = 1000$ K for all cases. Note that each pressure and temperature condition is the same as in Figure 7, respectively.

Path I	$H + O_2 + M \longrightarrow HO_2 + M$	$\Delta h_{1000\ K} = -47$ (kcal/mol)	(R9)
	$\underline{HO_2 + H \longrightarrow OH + OH}$	-37	(R11)
	$2H + O_2 \longrightarrow OH + OH$	-84	
Path II	$2(H + O_2 + M \longrightarrow HO_2 + M)$	-94	(R9)
	$HO_2 + HO_2 \longrightarrow H_2O_2 + O_2$	-42	(R14)
	$\underline{H_2O_2 + M \longrightarrow OH + OH + M}$	52	(R15)
	$2H + O_2 \longrightarrow OH + OH$	-84	
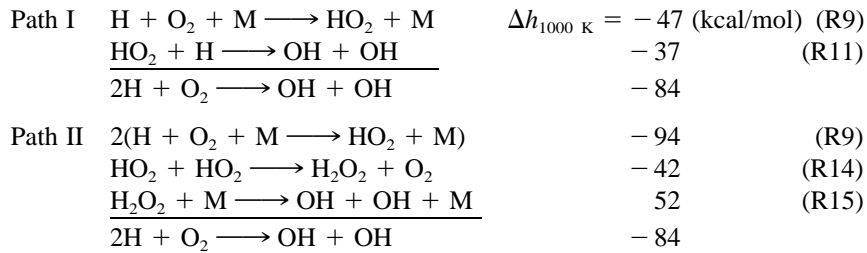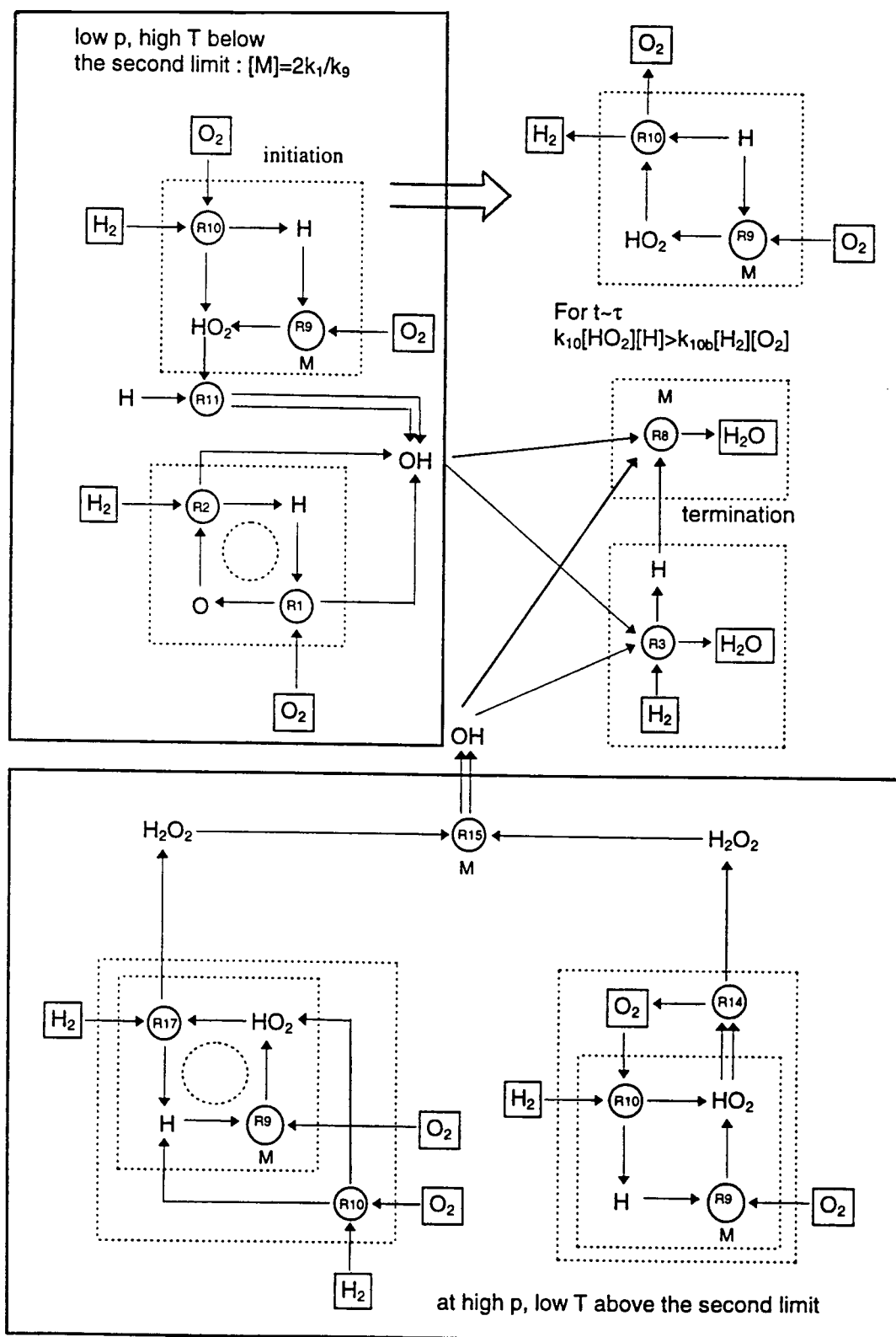
Figure 12   Main reaction paths for hydrogen oxidation (9 reactions). Dominant reactions are separated by the second limit criterion ([M] = 2 k_1/k_9). Refer to Table II for reaction numbers.
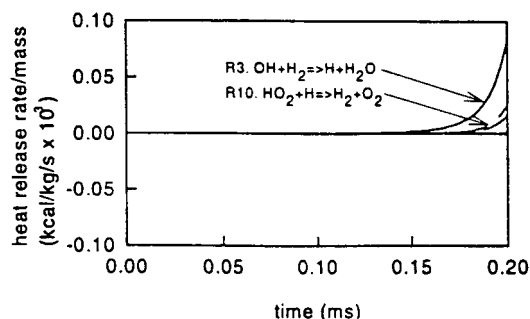
(a) p=0.1 MPa
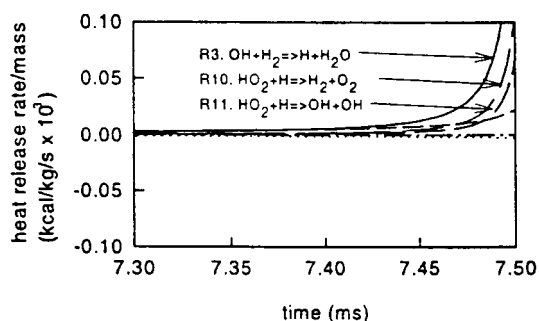
(b) p=0.3 MPa
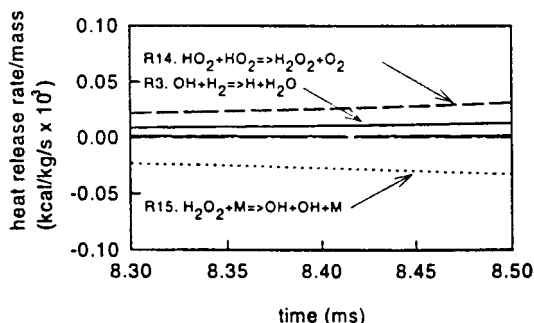
(c) p=1.0 MPa

Figure 13 Heat release rates (expressed as $\dot{w}_j \Delta h_j + r$ for each reaction j) for varying initial pressures before autoignition. (a) $p = 0.1$ MPa, (b) $p = 0.3$ MPa, and (c) $p = 1.0$ MPa. Initial temperature $T = 1000$ K for all cases. $H_2/O_2/Ar = 2/1/5$.

In both paths, the OH radical is finally consumed by the very exothermic reaction with H_2 (R3). Comparison of calculated induction times using isothermal and adiabatic conditions clearly shows the effect of reaction R14 on the overall progress of reaction at high pressures (Fig. 14).

COMPARISON BETWEEN MODEL AND EXPERIMENT

The use of the full thermodynamic model including heat loss and mass transfer to the crevice allows direct comparison of the calculated pressure histories with the experimental pressure measurements. The model, using the base chemical kinetic mechanism and rates in Table II, correctly captures the pressure drop due to heat loss during the induction period, as well as the pressure rise prior to autoignition (Fig. 15). However, predicted induction times are approximately one-half the measured values.

The sensitivity coefficients discussed in the previous section suggest that the candidate reactions responsible for the discrepancies are reactions R14, R15, and R17b. Figure 16 shows calculated induction time changes compared to the reference value when reaction rate constants for R14, R15, and R17b are varied within their estimated uncertainty factor. Reactions R14 and R15 have been more extensively investigated than reaction R17 [28,29,30]. Only low-temperature estimates (< 750 K) have been made for R17, and in most of those experiments, the sum of $k_{16} + k_{17}$ is measured, while the ratio of the two pathways is estimated. An additional factor contributes to the uncertainty in R17b: the uncertainty of about 1 kcal/mol in the heat of formation of HO_2. Since the rate constant is estimated in the forward direction, any uncertainty in the heat of formation directly affects the reverse reaction, thus the calculated values. Deviations in the calculated induction times due to difference in assumptions for third body efficiencies were not found to be greater than 15 percent.

The most reliable estimates for the total reaction rate for $H + H_2O_2$, $k_{16} + k_{17}$ are the low temperature (< 353 K) values measured by Klemm et al. [35] via flash photolysis-resonance fluorescence. The contribution of each channel as a function of temperature is still uncertain, especially at higher temperatures. Based on the bond energies involved, Klemm suggested that reaction R17 dominates at low temperatures, an approximation consistent with Baldwin et al.'s [36] estimate of a ratio of 0.125 for $k_{17}/(k_{16} + k_{17})$ at 773 K. Albers et al. [37] used deuterium to determine the ratio of the two channels, and concluded that R16 dominates at low temperatures, in contrast
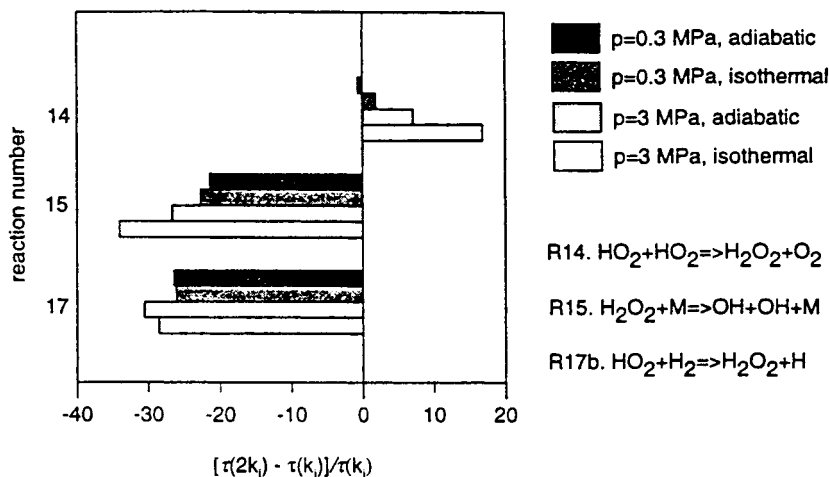
Figure 14 Induction time sensitivity comparison for reaction R14, R15, and R17b at different initial pressures. Initial temperature $T = 1000$ K for all cases.

with Klemm's assumption. Corrected rates for reaction with H (instead of D) have been recently reevaluated by Baulch et al. [38] as shown in Figure 17. The revised value for the sum of reactions is substantially lower than those by Klemm. However, it would seem unlikely that reaction R17 dominates at low temperatures, given the higher exothermicity and lower bond energies involved in R16.

An estimate for k_{17} can be made by determining the best fit parameters to assure that the estimate (a) includes previous measured data, (b) is within uncertainty ranges, and (c) is a best match to induction times measured in this study. An error minimization procedure was used in order to seek the optimum value of the parameters A and E for the relatively narrow range of temperatures and pressures considered, and for two extreme values of $\Delta h^0_{f,298.15\,K}(HO_2)$. Best agreement over all conditions studied is obtained by decreasing the preexponential factor recommended by Tsang and Hampson [24], while keeping the same activation energy (Fig. 17). The values agree with Baldwin et al.'s estimates for k_{17} [36], and are a factor of 2.1 lower than Tsang and Hampson's evaluation. The mean deviation from measured values using the reevaluated rate constant is about 20%. A comparison of the final predicted ignition delay times with experimental values is shown in Figure 18 for one particular contour of ignition delay time as a function of pressure and temperature. Notice that changes in the accepted values for the heat of formation of HO_2 only affect the absolute values of the predicted times, but not the slope with pressure and temperature.

Clearly, although the analysis shows good agree-

ment for a well tested set of reactions in the H_2—O_2 system, the current estimate would have to be reevaluated should drastic changes become necessary in reactions R14 and R15, to which induction times have comparable sensitivity. As an example, a 20% change in k_{15} by changing the pressure fit from a Lindeman fall-off fit to a Troe fit leads to a 10% increase in induction time. A thorough reevaluation of the best values for k_{17} and k_{16} (since they are often coupled) for a wide range of pressures and temperatures would be valuable, if enough data were available. The currently proposed revised rate is, on the basis of the present measurements and analysis, the best measurement for k_{17} at high temperatures and pressures.

CONCLUSION

The autoignition of hydrogen-oxygen mixtures at pressures above the second explosion limit (0.6–4.0 MPa) was investigated in a rapid compression machine. A special piston crevice was created for this rapid compression machine to allow accurate characterization of mixture temperature in the reacting zone in chemical kinetic studies. A thermodynamic model, including the effects of heat transfer and early heat release was combined with a detailed chemical kinetic model for direct comparisons with the experimental data. The analysis of the reaction fluxes and sensitivities leads to the following conclusions regarding hydrogen-oxygen reactions at pressures above the second explosion limit: (1) The evolution of the reaction is dominated by the fate of the HO_2 radical. In

(a) T_{max}=963 K

(b) T_{max}=1000 K

(c) T_{max}=1040 K
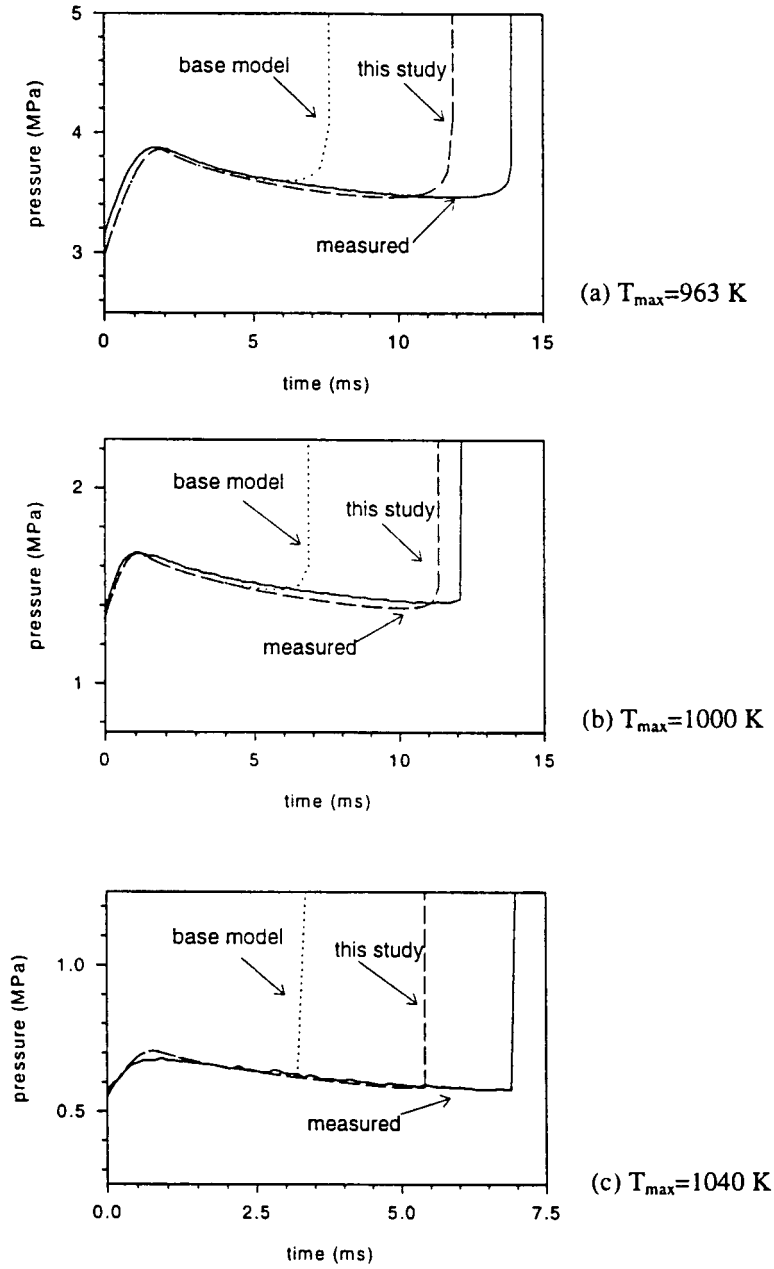
Figure 15 Measured and calculated pressure histories.
—— Measured by this work;
------- base model (Kim et al. [17]); where $k_{17} = 4.79 \times 10^{13}\exp(-7950/RT)$ (Tsang et al. [24]); and
------- this study with $k_{17} = 2.3 \times 10^{13}\exp(-7950/RT)$ (see text).

Figure 16 Comparison of calculated induction time change for changes in rate constants within their respective estimated uncertainty factor from the base model (Table II). Reference case: $L/H = 8.2/0.6$ cm; $p_o = 93.3$ kPa; and $T_o = 294$ K.
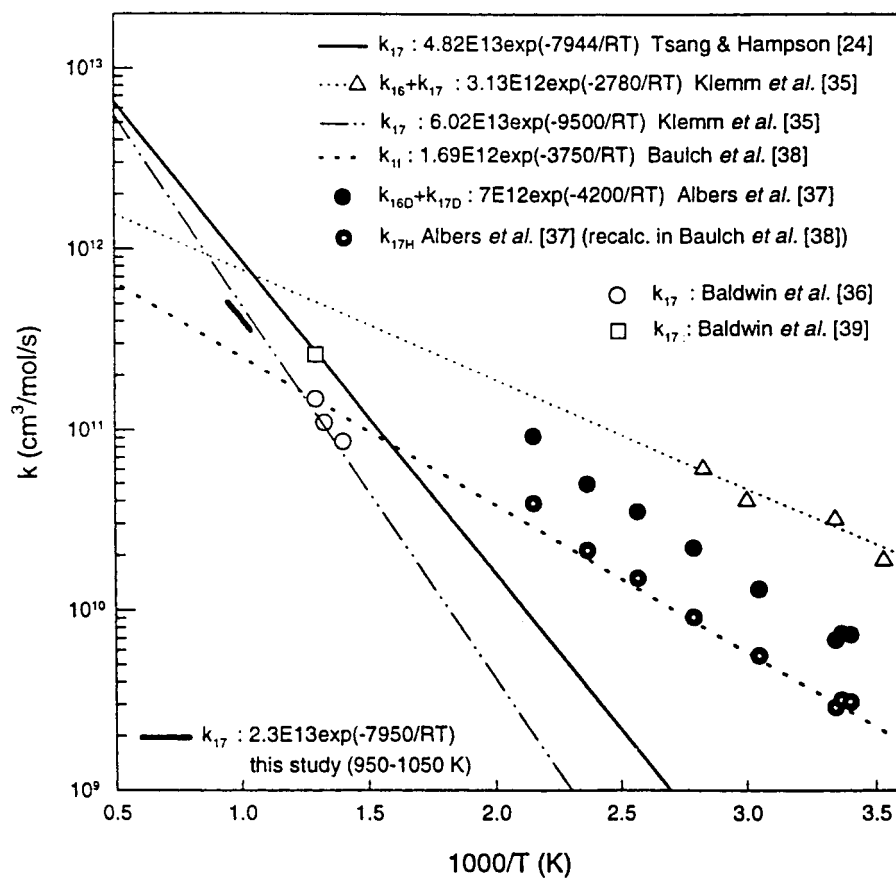
Figure 17 Comparison of reaction rate constants for R17.
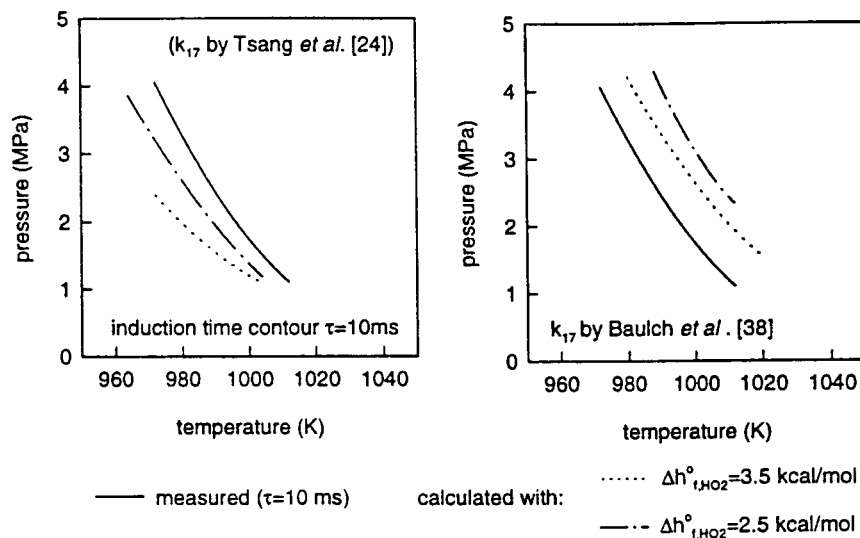
(a) Effect of heat of formation of HO_2 on calculated time contour

(b) Calculated induction time contours for different estimates of k_{17}

Figure 18   Comparison between measured and calculated induction time contours for different values of heat of formation for HO_2 (a) and reaction rate constants k_{17} (b).

particular, the competition between reactions R14 ($HO_2 + HO_2 \rightarrow H_2O_2 + O_2$), which is very exothermic, but consumes two radicals to produce H_2O_2, and R17b ($HO_2 + H_2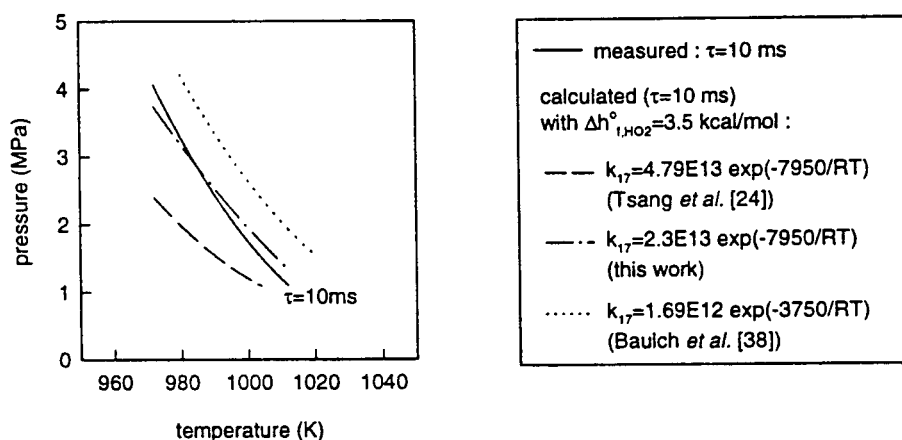 \rightarrow H_2O_2 + H$), which efficiently produces H_2O_2 from a single HO_2 radical. The rate constant for R17b was identified as one of the most important reactions for hydrogen oxidation at pressures above the second explosion limit and (2) Analysis of the previous estimates for k_{17}, as well as a best fit analysis for the present data suggests that a better expression for the high temperature values of k_{17} is given by $k_{17} = 2.3 \cdot 10^{13} \exp(-4000/T)$. This value

is a factor of 2.1 lower than the evaluation of Tsang & Hampson [24], and within the stated uncertainties from previous measurements. Induction times and energy release rates calculated using the modified reaction rate agree well (within 20 percent) with the measured values.

APPENDIX

Table A.I   Measurement Conditions and Results (H$_2$/O$_2$/Ar = 2/1/5)

No.	p_0 (mmHg)	T_0(K)	p_{max} (MPa)	T_{max} (K)	L (cm)	H (cm)	τ (ms)[a]
1	700	293.5	3.038	967.3	7.8	0.62	25.5
2	700	293.5	3.057	969.3	7.8	0.62	21.2
3	900.1	294	3.871	966	7.8	0.62	14
4	899.9	294	3.844	963.8	7.8	0.62	14.6
5	700.2	294	3.165	982.3	8	0.62	10.6
6	500.2	294	2.239	978.9	8	0.62	23.1
7	500.3	293.5	2.316	988.5	8.28	0.62	13.1
8	400	293.5	1.938	1003.6	8.70	0.62	8.3
9	225.1	294	1.091	1005.6	9.13	0.62	16.7
10	215	294	1.039	1004.3	9.13	0.62	24.2
11	200.7	293.5	0.999	1012.7	9.55	0.62	13.6
12	200.1	295	1.011	1022.9	9.55	0.62	5.7
13	200.1	295.3	0.985	1014.8	9.55	0.62	6
14	160.1	295.3	0.799	1019.6	9.55	0.62	7
15	160	295.2	0.791	1016.3	9.55	0.62	13.3
16	155.1	295.3	0.767	1016.5	9.55	0.62	16.7
17	155.1	295.3	0.75	1008.9	9.55	0.62	10.1
18	210.1	295.5	1.105	1038.3	9.55	0.62	3.9
19	200.1	295.5	1.007	1023.2	9.55	0.62	5.1
20	199.9	295.3	1.042	1034.2	9.76	0.62	3.5
21	200.1	293.8	1.045	1030.3	9.76	0.62	5.7
22	200.2	294.1	1.046	1031.2	9.76	0.62	6
23	180.1	294.5	0.931	1028.9	9.76	0.62	9
24	180.1	294.7	0.936	1031.6	9.76	0.62	7.5
25	180.1	294.9	0.937	1032.4	9.76	0.62	7.8
26	150.2	297	0.797	1046.3	9.9	0.62	4.4
27	130	296.6	0.678	1039	9.9	0.62	6.9
28	130.1	297	0.677	1039.8	9.9	0.62	6.4
29	120.1	297	0.615	1034.5	9.9	0.62	9
30	120.1	297.2	0.618	1036.6	9.9	0.62	6.4
31	109.9	296.9	0.569	1037.4	9.9	0.62	2.7
32	120.1	297	0.614	1033.4	9.9	0.62	7.2

[a] Induction times τ measured from steepest slope (0.9 ± 0.3 ms earlier than peak pressure) for each experiment. Error represents repeatability bounds.

Table A.II   Summary of Derived Model Equations

Equation	Description	Remarks

(i) Core

$dm_\infty = -d(m_\delta + m_c)$ — mass conservation — eq. (2)

$dV_\infty = dV - dV_\delta$ — volume conservation — eq. (3)

$dU_\infty = -pdV_\infty + h_\infty dm_\infty$ — energy conservation — eq. (4)

$dU_\infty = d(m_\infty u_\infty)$ — internal energy — eq. (5)

$u_\infty = \sum_{i=1}^{K} h_i Y_i - \dfrac{p}{p_\infty}$ — specific internal energy — eq. (6)

$h_i = h_i^0 + \int_{T_0}^{T_\infty} c_{p,i} dT$ — specific enthalpy — eq. (7)

$\dfrac{dY_i}{dt} = \dfrac{\dot{w}_i M_i}{p_\infty}$ — species equation[a] — eq. (8)

$m_\infty = p_\infty V_\infty = \dfrac{p}{R_\infty T_\infty} V_\infty$ — core mass (state equation) — eq. (9)

(ii) Thermal Boundary Layer

$dU_\delta = \delta Q - p\, dV_\delta - h_\infty\, dm_\infty - h_c\, dm_c$ — energy conservation — eq. (10)

$\delta Q = -k_t A(y) \left.\dfrac{dT}{dy}\right|_{y=0} dt$ — heat conduction — eq. (11)

$m_\delta = p_\delta A \delta_t = A \int_0^{\delta_t} \dfrac{p}{RT} dy$ — boundary layer mass — eq. (12)

$h_\delta = \dfrac{A}{m_\delta}\int_0^{\delta_t} p c_p T\, dx = \dfrac{pA}{m_\delta}\int_0^{\delta_t}\dfrac{y}{y-1} dy$ — average boundary layer enthalpy — eq. (13)

(iii) Crevice

$m_c = \dfrac{V_c}{RT_0} p$ — state equation — eq. (14)

$h_c \equiv \begin{cases} h_\delta\, dm_c > 0 \\ h_0\, dm_c < 0 \end{cases}$ — enthalpy of mass exchanged with crevice — eq. (15)

Equations to be solved

Equation — Dependent variables

$\left(\dfrac{V_\infty}{V} + \dfrac{V_\delta}{V}\dfrac{T_\infty}{T_\delta} + \dfrac{T_\infty}{T_0}\dfrac{V_c}{V}\right)\dfrac{dp}{p} - \dfrac{V_\infty}{V}\dfrac{dT_\infty}{T_\infty} - \dfrac{V_c}{V}\dfrac{T_\infty}{\overline{T}_\delta}\dfrac{d\overline{T}_\delta}{\overline{T}_\delta} + \left(1 - \dfrac{T_\infty}{\overline{T}_\delta}\right)\dfrac{dV_\infty}{V} + \dfrac{T_\infty}{T_0}\dfrac{dV_c}{V} = 0$ — p, T_∞, δ_t

$\left[\left(\dfrac{1}{\gamma-1}\right)_\delta \dfrac{V_\delta}{V} + \left(\dfrac{\gamma}{\gamma-1}\right)_\infty \dfrac{V_\infty}{V} + \left(\dfrac{\gamma}{\gamma-1}\right)_c \dfrac{T_c}{T_0}\dfrac{V_c}{V}\right]\dfrac{dp}{p} + \left(\dfrac{\gamma}{\gamma-1}\right)_\delta \dfrac{dV_\delta}{V} +$ — p, T_∞, δ_t

$\left(\dfrac{\gamma}{\gamma-1}\right)_\infty \dfrac{dV_\infty}{V} - \left(\dfrac{\gamma}{\gamma-1}\right)_\infty \dfrac{V_\infty}{V}\dfrac{dT_\infty}{T_\infty} + \left(\dfrac{\gamma}{\gamma-1}\right)_c \dfrac{T_c}{T_0}\dfrac{dV_c}{V} = -\dfrac{1}{pV}k_w A(y)\left.\dfrac{dT}{dy}\right|_{y=0} dt$

Reacting Case:

$d\left[\left(\sum_{i=1}^{K} h_i^0 + \int_{T_0}^{T_\infty} c_{p,i} dT\right) Y_i\right] = c_{p,\infty} dT_\infty + \sum_{i=1}^{K} h_i^0 dY_i = \dfrac{dp}{\rho_\infty}$ — p, T_∞, Y_i

$\dfrac{dY_i}{dt} = \dfrac{\dot{w}_i M_i}{\rho_\infty}$ — Y_i

Nonreacting Case:

$c_{p,\infty} dT_\infty = \dfrac{dp}{\rho_\infty}$ or $\dfrac{dT_\infty}{T_\infty} = \dfrac{\gamma(T_\infty)-1}{\gamma(T_\infty)}\dfrac{dp}{p}$ — p, T

[a] The molar rate per unit volume was calculated from $\dot{w}_i = \sum_{j=1}^{K} \dot{w}_j$, where $\dot{w}_j$ are the reaction rates for all reactions involving species j; $\dot{w}_j$ is calculated from the reaction rate constant k_j and concentrations involved in reaction j.

BIBLIOGRAPHY

1. S. G. Saytzev and R. I. Soloukin, *Eighth Symposium (Int'l) on Combustion,* Williams and Wilkins, 1962, p. 344.

2. R. A. Strehlow and A. Cohen, *Phys. Fluids,* **5,** 97 (1962).

3. G. B. Skinner and G. H. Ringrose, *J. Chem. Phys.,* **42**(6):2190 (1965).

4. J. W. Meyer and A. K. Oppenheim, *Thirteenth Symposium (Int'l) on Combustion,* The Combustion Institute, 1971, p. 1153.

5. W. Kordylewski and S. K. Scott, *Combust. Flame,* **57**: 127–139 (1984).

6. P. Gray and M. E. Sherrington, *J. Chem. Soc., Far. Trans I*, **70**:2336 (1974).

7. R. A. Yetter, H. Rabitz and R. M. Hedges, *Int. J. Chem. Kin.*, **23**:251–278 (1991).

8. G. L. Schott and J. L. Kinsey, *J. Chem. Phys.*, **29**:1177 (1958).

9. R. K. Cheng, and A. K. Oppenheim, *Combust. Flame*, **58**:125–139 (1984).

10. E. L. Petersen, D. F. Davidson, M. Roehrig, and R. K. Hanson, *AIAA Paper* 95–3113, 31st AIAA/ASME/SAE/ASEE Joint Propulsion Conference and Exhibit, San Diego, 1995.

11. P. Park and J. C. Keck, *SAE Paper* 900027 (1990).

12. D. Lee and S. Hochgreb, Vortex Supression and Heat Transfer in Rapid Compression Machines, *Combust. Flame,* in press (1998).

13. M. Carlier, C. Corre, R. Minetti, J.-F. Pauwels, M. Ribaucour and L.-R. Sochet, *Twenty-Third Symposium (Int'l) on Combustion*, The Combustion Institute, 1753–1758, 1990.

14. M. P. Halstead, L. J. Kirsch and C. P. Quinn, *Combust. Flame*, **30**:45–60 (1977).

15. J. F. Griffiths, D. J. Rose, M. Schreiber, J. Meyer and K. F. Knoche, *Combust. Flame*, **91**:209–212, (1992).

16. J. F. Griffiths, Q. Jiao, M. Schreiber, J. Meyer, and K. F. Knoche, *Twenty-Fourth Symposium (Int'l) on Combustion*, The Combustion Institute, 1809–1815, 1992.

17. T. J. Kim, R. A. Yetter, and F. L. Dryer, *Twenty-fifth Symposium (Int'l) on Combustion*, The Combustion Institute, 759–766, 1994.

18. R. K. Kee, F. M. Rupley, and J. A. Miller, The CHEMKIN Thermodynamic Database, *Sandia Report*: SAND80-8003, 1987.

19. G. S. Shum, and S. W., Benson, *J. Phys. Chem.*, **87**: 3479–3482 (1983).

20. A. N. Pirraglia, J. V. Michael, J. W. Sutherland, and R. B. Klemm, *J. Phys. Chem.*, **93**:282 (1989).

21. J. W. Sutherland, J. V. Michael, A. N. Pirraglia, F. L. Nesbitt, and R. B. Klemm, *Twenty-First Symposium (Int'l) on Combustion*. The Combustion Institute, 929, 1986.

22. J. V. Michael, and J. W. Sutherland, *J. Phys. Chem.*, **92**: 3853 (1988).

23. J. W. Sutherland, P. M. Patterson, and R. B. Klemm, *Twenty-Third Symposium (Intl'l) on Combustion*. The Combustion Institute, 51, 1990.

24. W. Tsang, and R. F. Hampson, *J. Phys. Chem. Ref. Data*, **15**:1087 (1986).

25. M. W. Slack, *Combust. Flame*, **28**:241–249 (1977).

26. D. L. Baulch, D. D. Drysdale, D. G. Horne, and A. C. Lloyd, *Evaluated Kinetic Data for High Temperature Reactions*, Butterworths, London, 1976.

27. C. J. Cobos, H. Hippler, and J. Troe, *J. Phys. Chem.*, **89**:342–349 (1985).

28. H. Hippler, J. Troe, and J. Willner, *J. Chem. Phys.*, **93**(3):1755 (1990).

29. J. Warnatz, in Combustion Chemistry. Gardiner, Jr, W. C., Ed., Springer-Verlag, New York, NY, 1985.

30. L. Brouwer, C. J. Cobos, J. Troe, H.-R. Dubal, and F. F. Crim, *J. Chem. Phys.*, **86**:6171 (1987).

31. H. Hippler, and J. Troe, *Chem. Phys. Lett.*, **192**:333 (1992).

32. C. K. Westbrook, and F. L. Dryer, *Prog. Ener. Combust. Sci.*, **10**:1–57 (1984).

33. J. C. Keck, *Letters in Heat and Mass Transfer*, **8**:313–319 (1981).

34. B. Lewis, and G. V. Elbe, Combustion, Flames and Explosions of Gases, Academic Press, 1987.

35. R. B. Klemm, W. A. Payne, and L. J. Stiff, *Int. J. Chem. Kin., Symp. No 1*, 61, (1975).

36. R. R. Baldwin, D. Brattan, B. Tunnicliffe, R. W. Walker, and S. J. Webster, *Combust. Flame*, **15**:133–142 (1970).

37. E. A. Albers, K. Hoyermann, H. G. Wagner, and J. Wolfrum, *Thirteenth Symposium (Int'l) on Combustion*. The Combustion Institute, 81, 1971.

38. D. L. Baulch, C. L. Cobos, R. A. Cox, C. Esser, P. Frank, Th. Just, J. A. Kerr, M. J. Pilling, J. Troe, R. W. Walker, and J. Warnatz, *J. Phys. Chem. Ref. Data*, **21**(3):411 (1992).

39. R. R. Baldwin, and R. W. Walker, *J. Chem. Soc., Far. Trans. I*, **75**:140 (1979).